Angewandte Chemie

Eine Zeitschrift der Gesellschaft Deutscher Chemiker

Nuclear Resonance Vibrational Spectroscopy on the $Fe^{IV}=O$ $S=2$ Non-Heme Site in TMG_3tren: Experimentally Calibrated Insights into Reactivity**

Shaun D. Wong, Caleb B. Bell III, Lei V. Liu, Yeonju Kwak, Jason England, E. Ercan Alp, Jiyong Zhao, Lawrence Que Jr., and Edward I. Solomon**

anie_201007692_sm_miscellaneous_information.pdf

Supporting Information

Full Reference for the Gaussian 03 program package:

Gaussian 03 (Revision C.02), M. J. Frisch, G. W. Trucks, H. B. Schlegel, G. E. Scuseria, M. A. Robb, J. R. Cheeseman, J. A. Montgomery, Jr., T. Vreven, K. N. Kudin, J. C. Burant, J. M. Millam, S. S. Iyengar, J. Tomasi, V. Barone, B. Mennucci, M. Cossi, G. Scalmani, N. Rega, G. A. Petersson, H. Nakatsuji, M. Hada, M. Ehara, K. Toyota, R. Fukuda, J. Hasegawa, M. Ishida, T. Nakajima, Y. Honda, O. Kitao, H. Nakai, M. Klene, X. Li, J. E. Knox, H. P. Hratchian, J. B. Cross, V. Bakken, C. Adamo, J. Jaramillo, R. Gomperts, R. E. Stratmann, O. Yazyev, A. J. Austin, R. Cammi, C. Pomelli, J. W. Ochterski, P. Y. Ayala, K. Morokuma, G. A. Voth, P. Salvador, J. J. Dannenberg, V. G. Zakrzewski, S. Dapprich, A. D. Daniels, M. C. Strain, O. Farkas, D. K. Malick, A. D. Rabuck, K. Raghavachari, J. B. Foresman, J. V. Ortiz, Q. Cui, A. G. Baboul, S. Clifford, J. Cioslowski, B. B. Stefanov, G. Liu, A. Liashenko, P. Piskorz, I. Komaromi, R. L. Martin, D. J. Fox, T. Keith, M. A. Al-Laham, C. Y. Peng, A. Nanayakkara, M. Challacombe, P. M. W. Gill, B. Johnson, W. Chen, M. W. Wong, C. Gonzalez, and J. A. Pople, Gaussian, Inc., Wallingford, CT, 2004.

All Gaussian 03 calculations were performed using two common functionals: (i) BP86, which applies Becke's 1988 exchange functional[1] and Perdew's 1986 non-local correlation functional,[2] and (ii) the hybrid functional B3LYP, which uses Becke's three-parameter exchange functional[3] and the non-local correlation of Lee, Yang and Parr.[4, 5] **1** and **2** were optimized using the Pople triple-ζ basis set 6-311G* for the $S = 1$ and $S = 2$ states; for **1** the $S = 2$ state is more stable by 15.53 kcal/mol (BP86) or 18.40 kcal/mol (B3LYP), and for **2** the $S = 1$ state is more stable by 20.95 kcal/mol (BP86). Frequency calculations for NRVS spectral simulations were performed at the 6-311G* level on the optimized structures of **1** and **2**. The output files from these frequency calculations were processed with the gennrvs script rev. 57 (http://www.stanford.edu/group/solomon/software/gennrvs.txt) which uses the Fe displacements to derive mode composition factors and generate normalized PVDOS spectra (for details, see the Supporting Information of Ref. [14]). Note that for **1**, ^{1}H was substituted with ^{2}H on all terminal –CH$_3$ groups to reproduce the perdeuteration of the experimental samples.

For the reaction coordinates, geometry optimizations and frequency calculations were performed with the functional B3LYP and the double-ζ basis set LanL2DZ (for **1** and **2**) or an LACVP-equivalent (for **1$_t$**). Single-point energies were calculated for the optimized geometries using the larger triple-ζ basis set 6-311+G*, with direct inclusion of solvation effects using the Polarized Continuum Model and CH$_3$CN as the solvent.

1, (TMG3tren)Fe^{IV}=O	Fe—O (Å)	Average Fe—N$_{eq}$ (Å)	Fe—N$_{ax}$ (Å)	Guanidino C—N (Å)
BP86/6-311G* Opt	1.645	2.026	2.119	1.355/1.360/1.372
B3LYP/6-311G* Opt	1.622	2.037	2.129	1.346/1.352/1.363
X-ray crystallography	1.661(2)	2.005	2.112(3)	1.347/1.358/1.335
EXAFS	1.64	1.99		N/A
2, (N4Py)Fe^{IV}=O	Fe—O (Å)	Fe—N$_{eq}$ (Å)	Fe—N$_{ax}$ (Å)	Equatorial angles (°)
BP86/6-311G* Opt	1.643	1.972/1.976	2.075	89/91/86/91
X-ray crystallography	1.639	1.949/1.964	2.003	86/92/89/92
EXAFS	1.68	1.98		N/A

From crystallography, **2** has 2 pyridines canted 14° and 2 pyridines canted 21° from the Fe—O axis (Ref. [6])

Table S1. Structural parameters of **1** and **2** from DFT, X-ray crystallography and EXAFS.
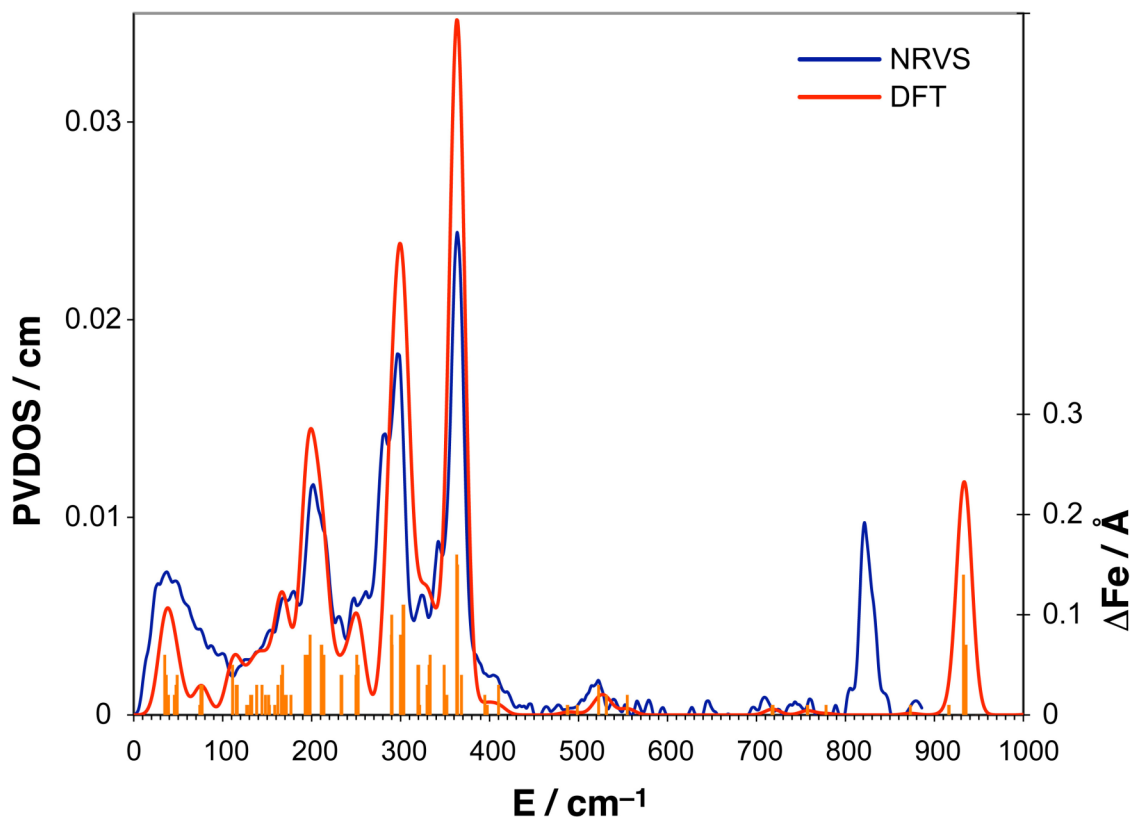

Figure S1. DFT-predicted PVDOS (blue) of **1** at the B3LYP/6-311G* level, overlaid with NRVS data (blue). Fe displacements shown as orange bars.
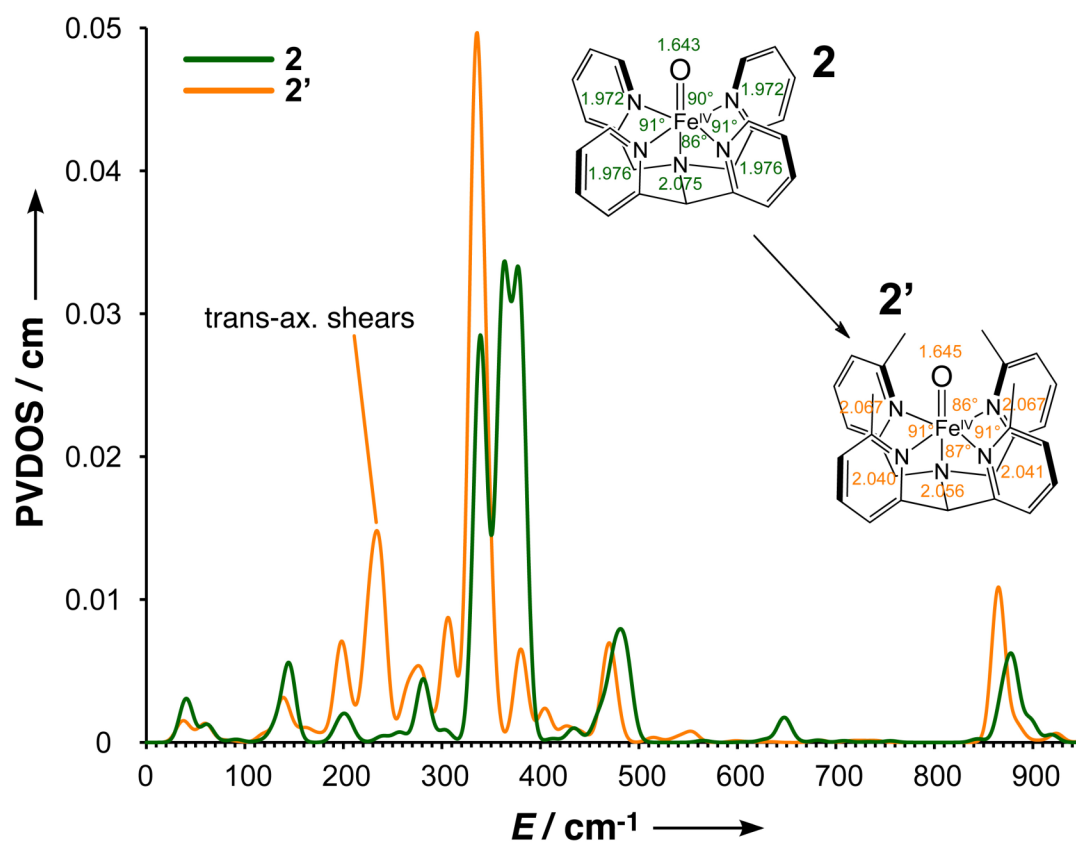
Figure S2. Comparison of DFT-calculated NRVS spectra of **2** (green) and **2'** (orange), which has *ortho* methyl substituents on the pyridine rings forming a steric wall around the oxo moiety. The steric wall causes the growth of a new peak corresponding to the *trans*-axial shears. Note that the three most-intense peaks in **2** (*trans*-axial bends and *trans*-axial stretch) are now subsumed under the peak at ~ 350 cm^{-1} in **2'**. In addition, the *trans*-axial bends of **2'** have lost one-third of their intensity as compared to **2**, and this was transferred to the *trans*-axial shears.
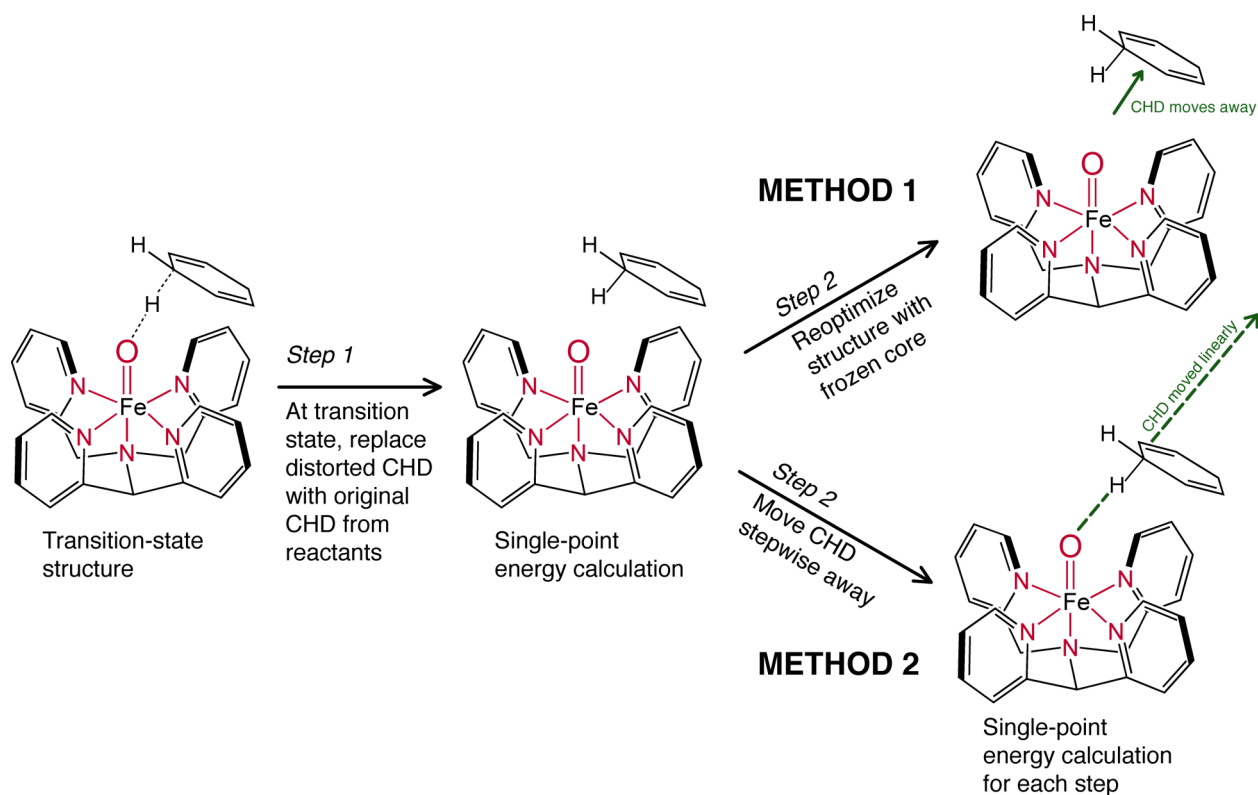
Scheme S1. Procedures used to estimate steric contribution to total reaction barrier starting from the transition state, as illustrated for **2**. (i) In method 1, the deformed CHD with a partially-broken C–H bond at the transition-state structure is replaced by the original undeformed CHD from the reactant structure, at the transition-state substrate orientation and C---O distance. This gives the total steric and electronic contributions to the energy required to reach the transition state without partially-breaking the C–H bond; this decreases the energy by 0.8 kcal/mol for **1** and 0.4 kcal/mol for **2**. Next, all Fe—L bonds in red were frozen while the other coordinates were allowed to optimize, which lowers the energy by decreasing the steric repulsion while maintaining the approximate electronic structure of the transition state. (ii) For method 2, the distorted CHD in the transition state was again replaced with the undistorted CHD and then moved away stepwise from the Fe^{IV}=O unit (without geometry optimization) – the energy of the entire system decreased to a minimum and rose again as the CHD moved further away.
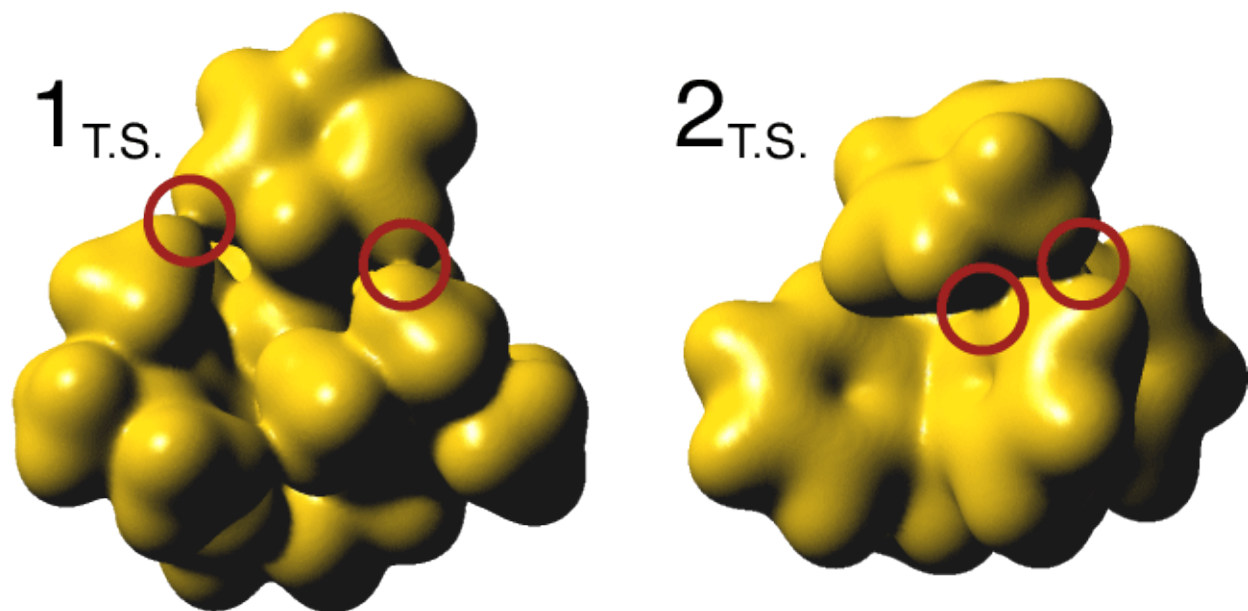
Figure S3. Electron density maps (at the same isosurface value) of transition state structures of **1** (left) and **2** (right), showing interaction of CHD electron density with the ligand electron density (red circles), representing the steric repulsion between CHD and ligand. For **1**, there are two interactions between the CHD C–H electron density and the TMG$_3$tren methyl groups. For **2**, there is an interaction between the CHD π-electron density and the N4Py pyridine C–H and an interaction between the CHD methylene C–H and another N4Py pyridine C–H.
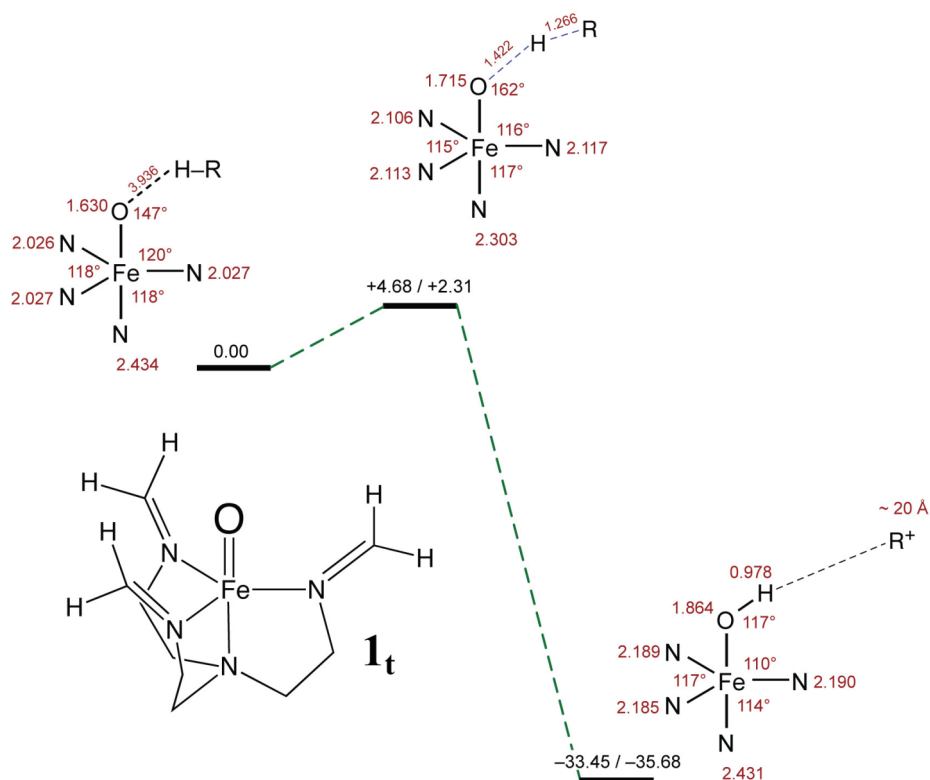
Figure S4. Reaction coordinate of truncated model (1_t, Ref. [19]) + CHD, with structure of 1_t in inset. Solvated energies ($\Delta E / \Delta G$) given in kcal/mol. Key geometrical parameters of reactant, transition state and product complexes given in red, with distances in Å.

Product species	1		1_t	
	ΔE	ΔG	ΔE	ΔG
Fe^{III}–OH $S = 1/2$	+14.75	+13.15	−5.38	−4.08
Fe^{III}–OH $S = 3/2$	−4.65	−7.11	−26.36	−27.41
Fe^{III}–OH $S = 5/2$	*−12.59*	*−14.88*	−16.43	−19.15
Fe^{II}–OH $S = 2$	−2.64	−10.25	*−38.12*	*−44.48*

Table S2. Solvated reaction energies (kcal/mol, B3LYP/6-311+G*) for the two possible reactions: (i) H-atom abstraction (Fe^{IV}=O + R–H → Fe^{III}–OH + R˙) and (ii) hydride abstraction (Fe^{IV}=O + R–H → Fe^{II}–OH + R$^+$) comparing reactant Fe^{IV}=O species **1** and 1_t (R–H = CHD, each component optimized separately with B3LYP/LanL2DZ). The large difference in reactivity results from decreased ligand donation to the Fe center in 1_t relative to **1**, thereby raising the Fe^{II}/Fe^{III} redox potential of 1_t relative to **1**. The $Fe^{III} → Fe^{II}$ reduction $\Delta G°$ is +4.63 kcal/mol for **1** and −17.07 kcal/mol for 1_t, making the Fe^{III}/Fe^{II} redox potential 21.70 kcal (~ 0.94 eV) higher for 1_t.
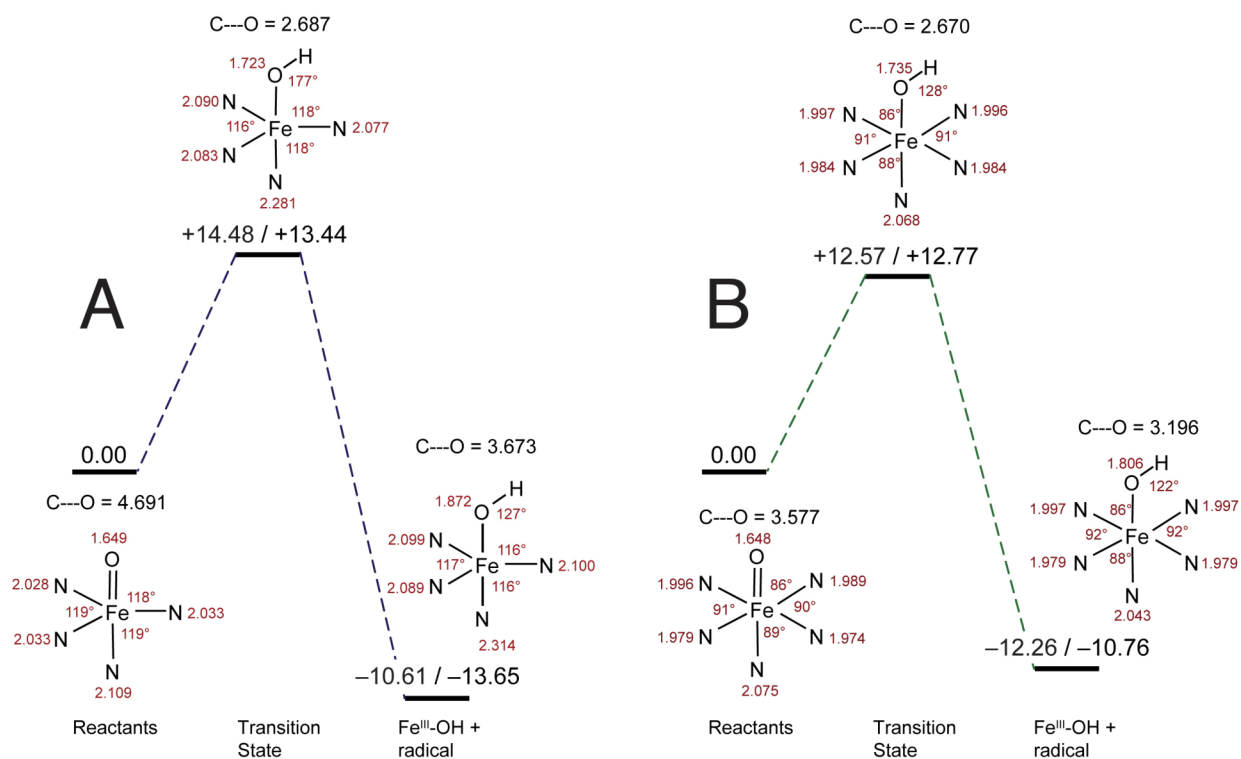
Figure S5. Reaction coordinates of A) **1** and B) **2** with CHD, showing key geometrical parameters of reactant, transition state and product complexes, with distances in Å. Solvated energies ($\Delta E/\Delta G$) given in kcal/mol.